Direct numerical simulation of strong shock-turbulent boundary layer interaction

Yujoo Kang[1], Sang Lee[2]

Abstract

This study investigates shock-turbulent boundary layer interaction (STBLI) over a $24°$ compression ramp at Mach 2.9 using direct numerical simulation. An in-house code based on a compact finite difference scheme is introduced and validated. Two distinct turbulent kinetic energy hotspots are identified: one near the wall behind the separation point and another in the free shear layer near the reattachment point. A significant factor contributing to the second amplification phenomenon is elucidated, involving the cluster of shocklets near the reattachment point. Analysis of pressure fluctuation power spectral density reveals concentrated high-pressure fluctuation regions near both separation and reattachment points, with distinct low and mid-to-low frequency phenomena observed, particularly near the separation point.

Keywords: Shock-turbulent boundary layer interaction, Computational fluid dynamics, Direct numerical simulation, Supersonic flow, Turbulent

Nomenclature

u – Streamwise velocity component
v – Wall-normal velocity component
w – Spanwise velocity component
p – Pressure
ρ – Density
M – Mach number
T – Temperature
C_f – Skin friction coefficient
δ – Boundary layer thickness
θ – Momentum thickness
St – Strohaul number

$<>$ – Favre averaging operator

Superscripts
- – Reynolds averaging operator

Subscripts
∞ – Free stream parameters
0 – Parameters at reference station
w – Wall parameters
$\perp$ – wall-normal coordinates
` – Fluctuation

1. Introduction

   The interaction between shockwaves and turbulent boundary layers, known as shock-turbulent boundary layer interaction (STBLI), holds a critical significance for high-speed vehicles that can have negative effects. When the shock wave penetrates the turbulent boundary layer, the adverse pressure gradient results in flow separation. The separated flow is associated with large-scale, low-frequency unsteadiness. STBLI manifests a spectrum of adverse consequences on vehicle performance, encompassing loss of control authority, pressure drops, surface unsteadiness, and even engine unstart [1-2]. Given the paramount importance of comprehensive physical investigations and precise

---

[1] *Korea Advanced Institute of Science and Technology, Daejeon, South Korea, ky5731@kaist.ac.kr*
[2] *Korea Advanced Institute of Science and Technology, Daejeon, South Korea, slee1@kaist.ac.kr*

estimations of STBLI in the design of high-speed vehicles, research in this domain has persevered over several decades. However, despite sustained efforts, the underlying mechanism of STBLI unsteadiness has been the subject of ongoing debate [1].

Since the early 2000s, the direct numerical simulation (DNS) of STBLI has been a subject of extensive research [3], aimed at unveiling the intricate mechanisms. Achieving accurate physical insights necessitates simulations of high-order and high-accuracy. In the perspective of fluid dynamics, the STBLI results complex phenomena, including flow separation, the creation of vortex structures, and the turbulence amplification. Of particular interest is the thorough comprehension of complex flow features, owing to its direct correlation with the dynamics of STBLI.

In the early stage of DNS investigations, considerable attention was directed towards the free shear layer as a primary contributor to turbulence amplification, primarily due to the localization of maximum turbulent kinetic energy (TKE) within it [4-5]. Moreover, studies indicated that the local Kelvin-Helmholtz (K-H) instability along the free shear layer and the formation of large-scale vortices serve as sources of TKE amplification [6-7]. However, Fang et al. [8] countered this perspective by highlighting that the streamwise Reynolds stress attains its peak value within the near-wall region. They proposed that the deceleration of the mean flow induced by the primary shock wave drives turbulence amplification. This mechanism has been substantiated by several subsequent studies [9-11].

In strong STBLI, investigations from both experimental [12-13] and DNS studies [10,11,14] have identified two discernible phases of TKE amplification. The first occurs immediately following the separation shock, while the second is observed around the reattachment point. Kang and Lee [14] underscore the importance of shocklets in instances of strong STBLI. Their findings indicate that clusters of shocklets induce mean flow deceleration, thereby contributing to the second TKE amplification.

In this study, we conducted a comprehensive analysis of strong STBLI using long-duration, high-fidelity, and high-resolution DNS. The shock wave structures and TKE is observed to investigate the two stage of turbulence amplification. Furthermore, pressure fluctuations across the entirety of the STBLI region are examined to provide a comprehensive understanding of its dynamics.

2. Numerical Method

In the present study, the supersonic turbulent boundary layer at $M_\infty = 2.9$ over a $24°$ compression ramp is analyzed as depicted in Fig 1. The flow parameters are selected based on the experiment of Bookey et al. [15] and the comparison of these parameters is provided in Table 1. The DNS is conducted using an in-house code. The detailed description and validation of are provided in our prior work [11].
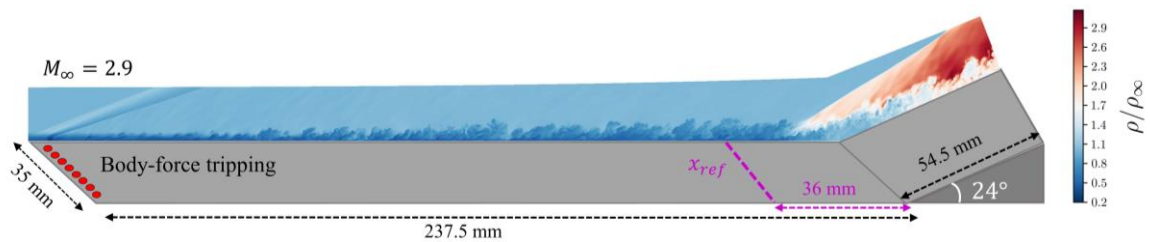

Fig 1. Flow configuration.

Table 1. Flow parameters of inflow turbulent boundary layer

	T_∞ (K)	T_w (K)	δ_0 (mm)	θ_0 (mm)	Re_θ	C_f
Bookey *et al.* [15] (Experiment)	107.1	307	6.6	0.43	2400	0.00225
Present DNS (in-house code)	107	307	6.6	0.43	2400	0.00227

The flow is governed by the fully three-dimensional unsteady compressible Navier-Stokes equations. The fluid under consideration is treated as a Newtonian fluid following Sutherland's law and Fourier's heat conduction law. Given the relatively low total enthalpy of the fluid, both calorically and the perfect gas equation are valid assumptions.

Spatial derivatives are computed using the sixth-order compact finite difference scheme originally developed by Lele [16]. Temporal integration is executed using the explicit 3rd-order Runge-Kutta method. After every final step in the Runge-Kutta method, an eight-order low-pass filter is applied to the solution vector to ensure numerical stability [17].

In order to mitigate spurious numerical oscillations, particularly in the vicinity of strong shock waves, a second-order low-pass filter is implemented. To identify the compression resulting from the shock, excluding the turbulent structure itself, a modified Ducros-type sensor is employed as a detector with a proper threshold [18]. Furthermore, artificial diffusivity, as formulated by Kawai and Lele [19], is employed to suppress unresolved high-frequency numerical fluctuations by diffusing the discontinuity present around the edges of turbulent structures.

The transition from laminar to turbulent boundary layer is achieved by the turbulent tripping method developed by Porter and Poggie [20], adding a counter-flow body force as a source term of the momentum and energy equation. The strength of the tripping force is significant since a large tripping force causes numerical instability and the small tripping force results longer streamwise length to obtain fully-developed turbulent.

The size of the computational domain is $L_x \times L_y \times L_z = 292 \times 71.7 \times 35.0 \ mm^3$ consisting with $N_x \times N_y \times N_z = 2865 \times 298 \times 420$ structured grid points. The reference station x_0 is positioned $36 \ mm$ ahead of the ramp corner, where the fully-developed turbulent boundary layer statistics are obtained. The grid resolution satisfies $\Delta x^+ = 4.6, \Delta y_w^+ = 0.42$, and $\Delta z^+ = 4.2$ which fall within the DNS resolution.

The laminar Blasius solution is injected as the inflow boundary, and the wall is treated as a non-slip isothermal wall with $T_w = 500 \ K$. The streamwise and wall-normal outlet values are extrapolated from the interior values. In the spanwise direction, periodic boundary condition is applied.

To investigate the low-frequency dynamics of STBLI, the log-time simulation is conducted. The physical simulation time is $1500 \delta_0/u_\infty$, which corresponds to $16.4 \ ms$ which is considerably longer than the previous DNS studies performed same flow configuration. Priebe et al. conducted $200 \delta_0/u_\infty$ [21] and $1000 \delta_0/u_\infty$ [22], and Wu and Martin [23], Kokkinakis et al. [14] and Shi and Yan [10] performed $300 \delta_0/u_\infty$ simulation.

3. Results

Fig 2. Shows the instantaneous and time-averaged contour of the non-dimensional density, streamwise velocity, and temperature on a side view. The main shock wave penetrates the turbulent boundary layer. Compared to the turbulent boundary layer, both density and temperature exhibit increments after encountering the primary shock wave. Two distinct compression stages are discernible: the first entails a strong and steep compression induced by the primary shock wave, while the second involves a more gradual and comparatively weaker compression. Furthermore, flow separation occurs around the corner of the ramp, characterized by instantaneous negative velocities, which persist even in the time-averaged contours. Notably, significant detachment is observed in instances of strong STBLI, whereas transient detachment is located in weaker instances of STBLI.
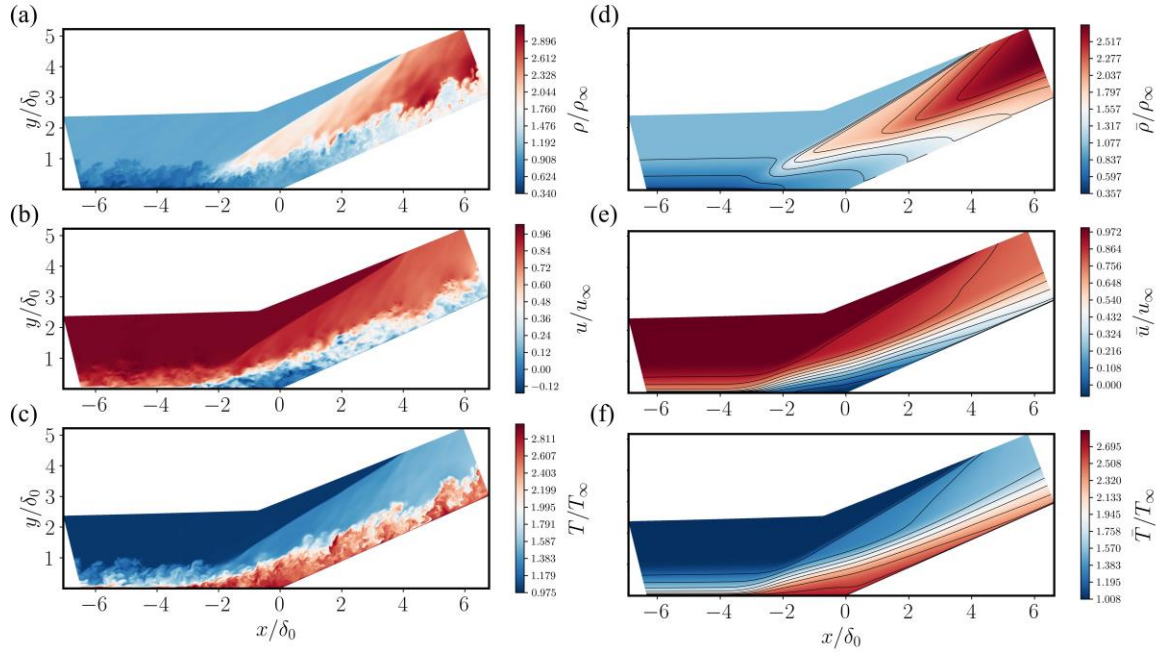
Fig 2. Instantaneous (a) density, (b) streamwise velocity, (c) temperature and (d)-(f) corresponding mean value, respectively.

The validity of the DNS results is established through a comparative analysis with experimental and other simulation data conducted under similar conditions, $Ma_\infty = 2.9$ turbulent boundary layer over $24°$ compression ramp. Fig 3 Presents the streamwise velocity profile at the reference station and $4\delta_0$ downstream of the ramp corner. Remarkably, the present DNS results precisely replicate the inflow turbulent boundary layer, exhibiting an excellent match with the experimental data [15]. Furthermore, the velocity profile aligns well with other DNS results [14,24]. Additionally, the velocity profile observed at $4\delta_0$ downstream of the ramp corner demonstrates good agreement with the experimental data [15]. Notably, the present DNS results exhibit better performance, particularly in the region proximate to the wall, when compared to other DNS results [23,25].
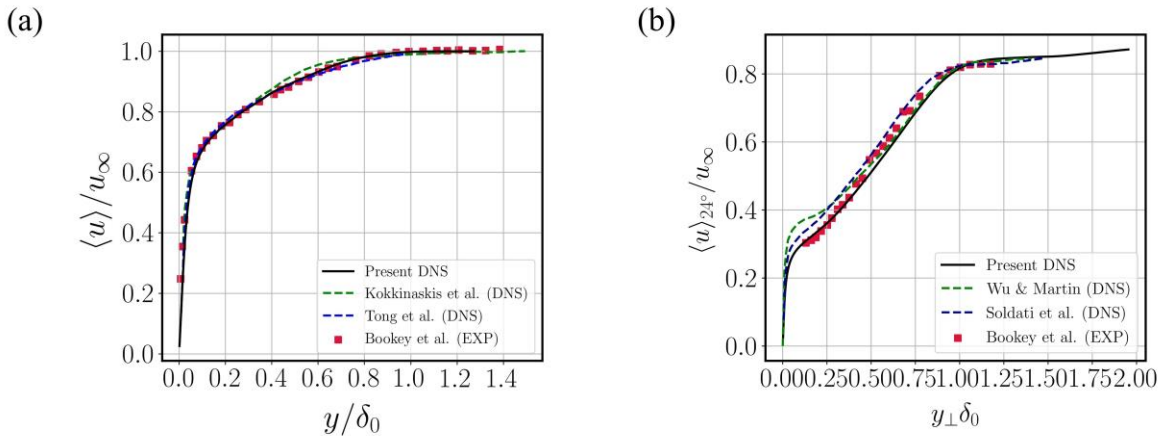

Fig 3. Streamwise velocity profile at (a) reference station and (b) $4\delta_0$ downstream of the ramp corner.

Fig 4 depicts the wall properties within STBLI alongside experimental data and other simulation data. Fig 4 (a) shows the streamwise distribution of the skin friction coefficient. The mean separation is defined as the regions characterized by negative skin-friction coefficients. Specifically, the separation point x_s is located in $x/\delta_0 \approx -3.13$ and the reattachment point x_r is observed at $x/\delta_0 \approx -1.50$. The separation length, denoted as L_s, is estimated to be approximately $4.63\delta_0$, representing the distance

between x_s and x_r. Notably, our DNS results closely align with the experimental data, in estimating the separation length.

In Fig 4 (b), the mean wall pressure distribution is presented, closely resembling the experimental data. Consistent with the observations in Fig 2, two distinct stages of pressure increase are discerned: the first occurring around the separation point and the second around the reattachment point.
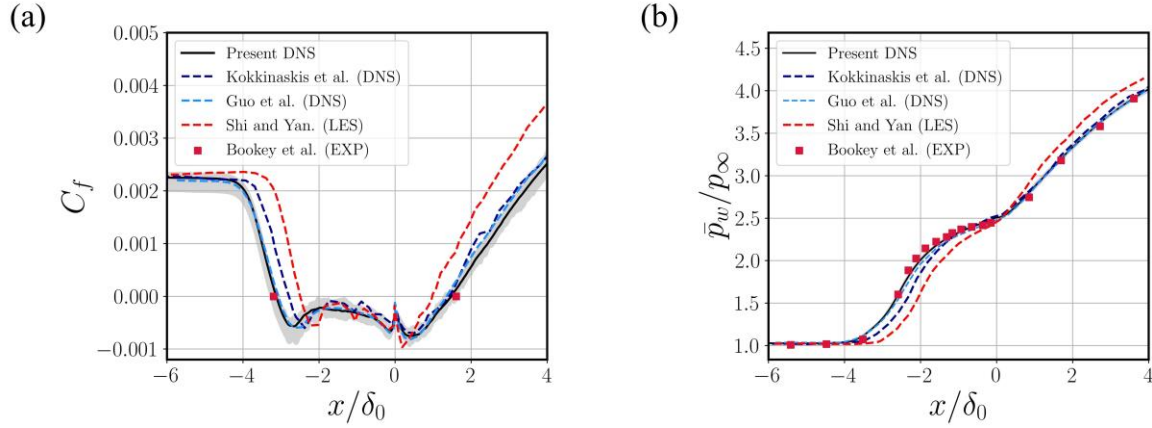

Fig 4. (a) Skin friction coefficient and (b) Wall pressure. Grey regions indicate the spanwise distribution.

The shock wave behavior within the STBLI is investigated. Fig 5 illustrates the numerical schlieren on side and frontal view at two time instant. The video of side view of schlieren is available in the online version of the previous study [11]. Notably, the main shock wave is prominently discernible, positioned within the shear layer. Following the main shock wave, a cluster of shock-wave branches, referred to as shocklets, emerges above the turbulent structures. These shocklets exhibit relatively weaker and convective characteristics compared to the main shock wave. Lee et al. [26] characterize these phenomena as eddy-shocklets, attributing them to shocks generated by the fluctuating fields of turbulent eddies. Indeed, the frontal view of Schlieren shows that the shocklets exhibit the concave shape, similar to the turbulent superstructures.

It is observed that the density gradient of the turbulent superstructures intensifies after the passage of the main shock wave. The shocklets from the fully-developed turbulent boundary layer exhibit lower density gradient magnitude compared to the turbulent structures. However, the shocklets get stronger rear the main shock.
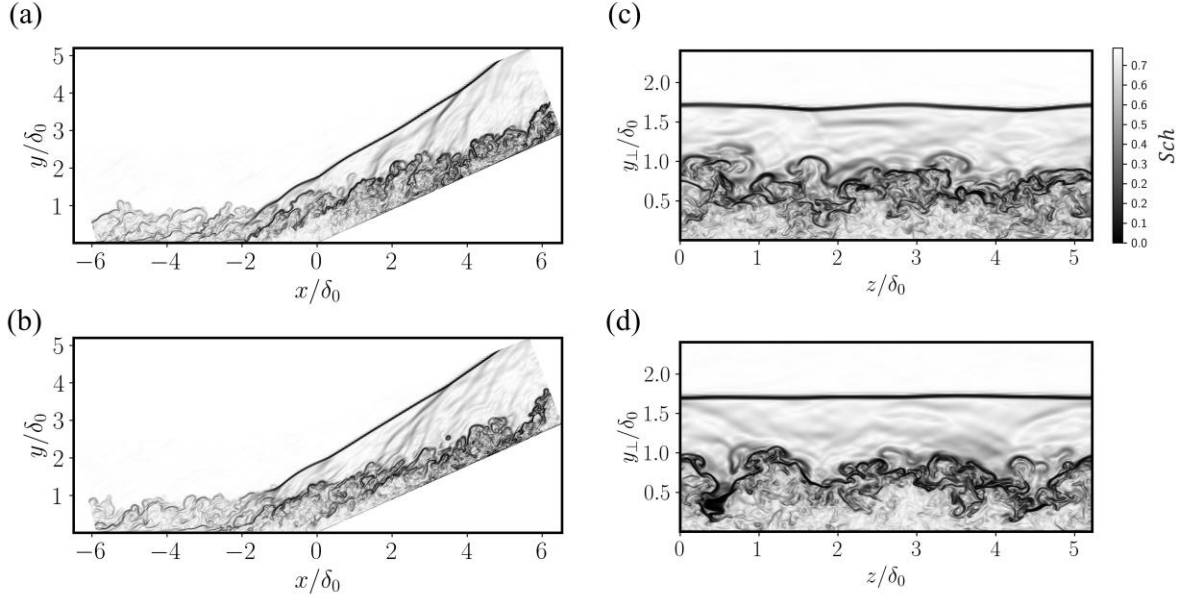
(a)

(c)

(b)

(d)

Fig 5. Numerical Schlieren at two time instant. (a)-(b): Side view and (c)-(d) frontal view
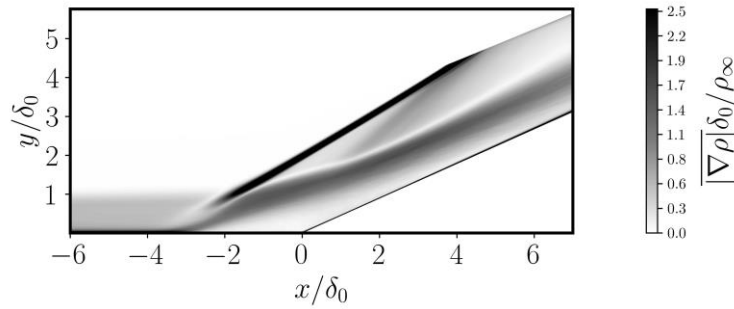
Fig 6. Normalized mean density gradient

Fig 6 shows the normalized mean density gradient. Four distinct regions are featured: (1) the shear layer of turbulent boundary layer, (2) the main shock wave, (3) the detached shear layer rear the main shock wave, and (4) the secondary shock wave. Although the shocklets have the intermittent and travelling motions revealed the overall region of STBLI, the mean density gradient shows the cluster of shocklets are concentrated and result the secondary shock wave.

Fig 7 shows the normal components of Reynolds stress $\langle u''u'' \rangle, \langle v''v'' \rangle, \langle w''w'' \rangle$ and TKE $k = \frac{1}{2}(\langle u''u'' \rangle + \langle v''v'' \rangle + \langle w''w'' \rangle)$ normalized with square of friction velocity u_τ^2. A comparison between the turbulent boundary layer and post-main shock reveals a notable disparity in the TKE level. The TKE experiences a substantial increase in the near-wall region just behind x_s, followed by an uplift above the separation bubble. This amplified TKE region experiences a rapid decay downstream of the main shock wave. Subsequently, a second TKE amplification is observed near x_r, followed by a decay process.

Previous studies showed that the first TKE amplification is induced by the mean flow deceleration. In addition, Shi and Yan [10] and Kang and Lee [11] reported that the flow acceleration above the separation bubble diminishes the TKE levels around the ramp corner. Also, Kang and Lee [11] highlights the flow deceleration due to the adverse pressure gradient induced by the cluster of the shocklets (secondary shock wave) resulting the second amplification of the TKE. Notably, while the first amplification primarily occurs in proximity to the wall, the second amplification is observed within the mixing layer.
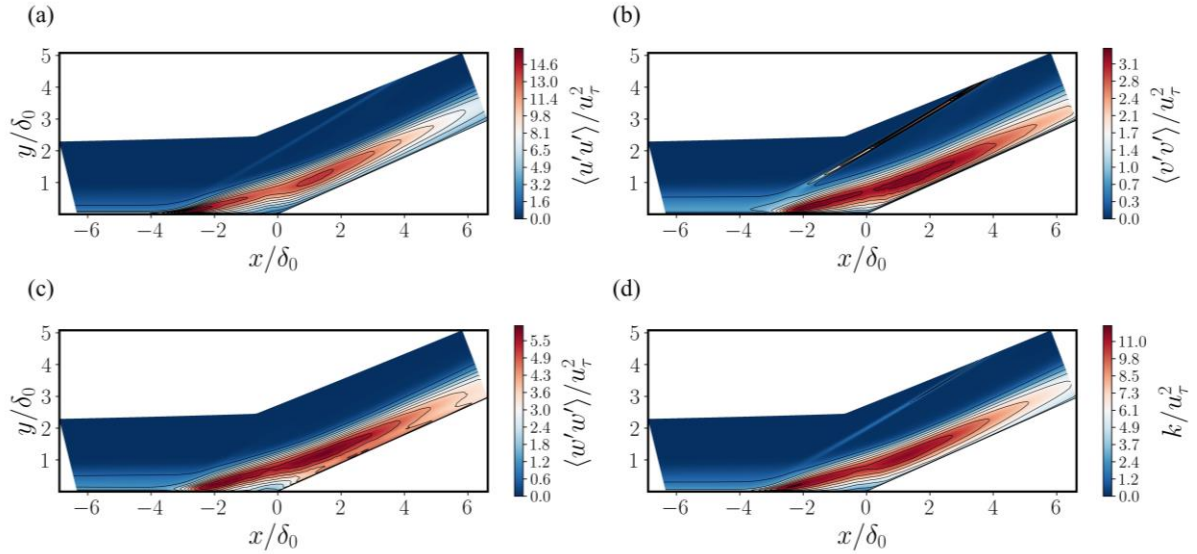
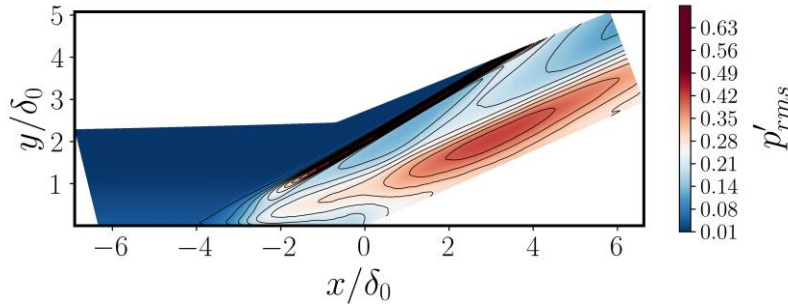**Fig 7.** (a)-(c): Normal components of Reynolds stress and (d) TKE.

Fig 8. Root mean square of pressure fluctuation.

Since shock motion and pressure fluctuations are related [27], the pressure fluctuation is observed. Fig 8 shows the contour plot of root mean square of pressure fluctuation. Three distinguishable high pressure fluctuating regions are observed. The region with the most intense pressure fluctuation is near the main shock. This is due to significant changes in flow before and after the main shock. Following this, another strong area is near the shear layer downstream of the main shock. This point is formed posterior to the reattachment point. While the secondary shock also exhibits high values of pressure fluctuation, its intensity is lower compared to the main shock.

The time signals of wall pressure are shown in Fig 9 (a) to illustrate the unsteadiness of STBLI. The data is acquired at four discrete positions, $x/\delta_0 \approx -5.4, -3.5, -2.5,$ and 1.5, correspond to the turbulent boundary layer, intermittent region, separation region, and reattachment point, respectively. A comparative analysis from the incoming turbulent boundary layer to within the STBLI region reveals the presence of low-frequency pressure fluctuations.

In Fig 9 (b), the power spectral density (PSD) of pressure fluctuation is presented. The frequency is normalized to both the Strouhal number based on the separation length $St_{L_s} = fL_s/u_\infty$ and the boundary layer thickness $St_{\delta_0} = f\delta_0/u_\infty$. Typically, in frequency domain analyses, normalization is conducted with respect to the shock length, as indicated in prior studies [22,28-30]. However, the normalization is often performed with respect to the boundary layer thickness [10,11,14]. Consequently, both scales are considered in Figs 9-10.

Relative to the turbulent boundary layer, the density of pressure fluctuation is heightened across the entirety of the STBLI region. Particularly noteworthy is the increased low-frequency unsteadiness observed after the separation point, notably around $St_{L_s} \approx 0.03$. This peak frequency aligns closely with

the range of $St_{L_s} = 0.02 \pm 0.01$ documented in previous literature [31, 32], encompassing experimental data from various configurations including unswept, swept, and axisymmetric compression ramps. Furthermore, long-term simulations in earlier studies [22,28,32,33] have reported characteristic low frequencies within the range of $0.02 < St_{L_s} < 0.05$, while short-term simulations [10,11,14] have identified a characteristic low-frequency at approximately $St_{\delta_0} \approx 0.02$. At the reattachment point, a broad-band mid-frequency content within the range of $0.1 < St_{L_s} < 3$ is evident. This observation is consistent with findings by Lee and Gross [29], who also investigated the presence of broad-band mid-frequencies spanning $0.1 < St_{L_s} < 3$.
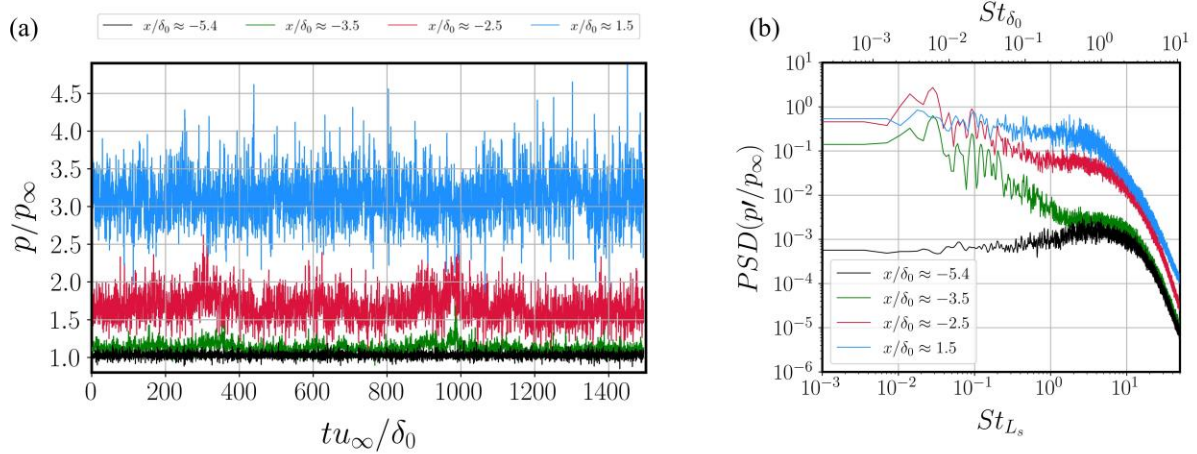

Fig 9. (a) Time series of wall pressure and (b) PSD of wall pressure fluctuation.

According to Kang and Lee [11], the region occupied by shocklets, unaffected by turbulent structures and shear layers, is characterized by mid-frequency phenomena. The second amplified TKE region is closely linked to the shocklet region due to the presence of characteristic mid-frequency motion in both areas.

Fig 10 illustrates the streamwise distribution of the PSD of pressure fluctuation, offering comprehensive insights into the overall dynamics of the STBLI. The analysis reveals a concentration of highly pressure-fluctuating regions within a short distance around the separation point and the wide region around and behind the reattachment point. Around the separation point, prominent PSD peaks of pressure fluctuation are observed at $St_{L_s} \approx 0.03$, indicative of low-frequency unsteadiness. Additionally, a substantial density of pressure fluctuation PSD is evident in the mid-to-low frequency range around $St_{L_s} \approx 0.1$.

Low-frequency dynamics are also notable around and behind the reattachment point, albeit weaker compared to the separation point. Similarly, a significant presence of mid-to-low frequency phenomena is observed in this region, akin to the separation point. However, around and behind the reattachment point, distinct broad-band mid-frequency phenomena are notable. According to Kang and Lee, corresponding mid-frequency is close to the characteristic frequency of shocklet region [11]. Such frequencies are not observed around the separation point due to the prominence of shocklets around and behind the reattachment point.
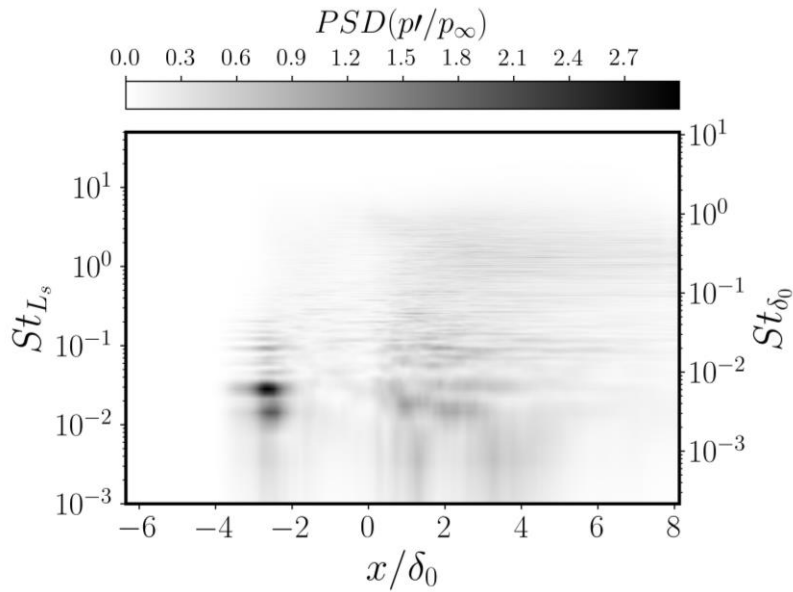
Fig 10. PSD of wall pressure fluctuation

4. Conclusions

In this study, a comprehensive DNS analysis to examine STBLI over a $24°$ compression ramp subjected to Mach 2.9 inflow conditions was conducted. An in-house code based on a compact finite difference scheme is introduced and the accuracy of the simulation was validated through comparisons with both numerical simulations and experimental data.

Within the strong STBLI system, two distinct TKE hotspots are observed. The first TKE hotspot arises in close proximity to the wall region situated behind the separation point, while the second hotspot is located within the free shear layer near the reattachment point.

Our investigation reveals an significant factor contributing to the phenomenon of second amplification. This phenomenon is characterized by the presence of clusters of shocklets emerging from prominent turbulent superstructure. The cluster of shocklets, accompanied by a secondary shock wave, induce an adverse pressure gradient, leading to flow deceleration near the reattachment point within the shear layer.

The PSD of wall pressure fluctuation is investigated to analyze the unsteadiness of STBLI. High pressure fluctuation regions are concentrated near the separation point and the reattachment point, with prominent low-frequency unsteadiness observed around $St_{L_s} \approx 0.03$ and mid-to-low frequency phenomena around $St_{L_s} \approx 0.1$ near the separation point. While low-frequency dynamics are present around and behind the reattachment point, they are weaker compared to the separation point. Around and behind the reattachment point, it is observed that the distinct broad-band mid-frequency phenomena attributed to shocklets in this region, which are absent around the separation point.

References

1. Clemens, N.T., Narayanaswamy, V.: Low-Frequency Unsteadiness of Shock Wave/Turbulent Boundary Layer Interactions. Annual Review of Fluid Mechanics. 46(1), 469-492 (2014)

2. Gaitonde, D.V.: Progress in shock wave/boundary layer interactions. Progress in Aerospace Sciences. 72, 80-99 (2015)

3. Adams, N.A.: Direct simulation of the turbulent boundary layer along a compression ramp at M = 3 and Reθ = 1685. Journal of Fluid Mechanics. 420, 47-83 (2000)

4. Smits, A.J., K.-C. Muck: Experimental study of three shock wave/turbulent boundary layer interactions. Journal of Fluid Mechanics. 182, 291-314 (1987)

5. Pirozzoli, S., Grasso, F.: Direct numerical simulation of impinging shock wave/turbulent boundary layer interaction at M=2.25. Physics of Fluids. 18(6), 065113 (2006)

6. Helm, C., Martin, M.P., and P. Dupont, P.: Characterization of the shear layer in a Mach 3 shock/turbulent boundary layer interaction. IOP Publishing (2014). https://doi.org/ 10.1088/1742-6596/506/1/012013

7. Li, X., Fu, D., Ma, U., Liang, X.: Direct numerical simulation of shock/turbulent boundary layer interaction in a supersonic compression ramp. Science China Physics. Mechanics and Astronomy. 53(9), 1651-1658 (2010)

8. Fang, J., Zheltovodov, A.A., Yao, C., Moulinec, C., Emerson, D.R.: On the turbulence amplification in shock-wave/turbulent boundary layer interaction. Journal of Fluid Mechanics. 897, A32 (2020)

9. Guo, T., Zhang, J., Tong, F., Li, X.: Amplification of turbulent kinetic energy and temperature fluctuation in a hypersonic turbulent boundary layer over a compression ramp. Physics of Fluids. 35(4), 046118 (2023)

10. Shi, J., Yan, J.: Turbulence amplification in the shock wave/turbulent boundary layer interaction over compression ramp by the flux reconstruction method. Physics of Fluids. 35(1), 016122 (2023)

11. Kang, Y. and Lee, S.: Direct numerical simulation of turbulence amplification in a strong shock-wave/turbulent boundary layer interaction. Physics of Fluids. 36(1), 016127 (2024)

12. Dupont, P., Piponniau, S., Dussauge, J.P.: Compressible mixing layer in shock-induced separation. Journal of Fluid Mechanics. 863, 620-643 (2019)

13. Pasquariello, V., Hickel, S., Adams, N.A.: Unsteady effects of strong shock-wave/boundary-layer interaction at high Reynolds number. Journal of Fluid Mechanics. 823, 617-657 (2017)

14. Kokkinakis, I.W., Drikakis, K., Ritos, K., Spottswood, S. M.: Direct numerical simulation of supersonic flow and acoustics over a compression ramp. Physics of Fluids. 32(6), 066107 (2020)

15. Bookey, P., Wyckham, C., Smits, A.: Experimental Investigations of Mach 3 Shock-Wave Turbulent Boundary Layer Interactions. American Institute of Aeronautics and Astronautics (2005). https://doi.org/10.2514/6.2005-4899

16. Lele, S.K., Compact finite difference schemes with spectral-like resolution. Journal of Computational Physics. 103(1), 16-42 (1992)

17. Gaitonde, D.V., Visbal, M.R.: Pade-Type Higher-Order Boundary Filters for the Navier-Stokes Equations. AIAA Journal. 38(11), 2103-2112 (2000)

18. Bernardini, M., Modesti, D., Salvadore, F., Pirozzoli, S.: STREAmS: A high-fidelity accelerated solver for direct numerical simulation of compressible turbulent flows. Computer Physics Communications. 263, 107906 (2021)

19. Kawai, S., Lele, S.K.: Localized artificial diffusivity scheme for discontinuity capturing on curvilinear meshes. Journal of Computational Physics. 227(22), 9498-9526 (2008)

20. Poggie, J.: Compressible turbulent boundary layer simulations: resolution effects and turbulence modeling. in 53rd AIAA Aerospace Sciences Meeting (2015)

21. Priebe, S., Tu, J.H., Rowley, C.W., Martin, M.P.: Low-frequency dynamics in a shock-induced separated flow. Journal of Fluid Mechanics. 807, 441-477 (2016)

22. Priebe, S., Martín, M.P: Low-frequency unsteadiness in shock wave–turbulent boundary layer interaction. Journal of Fluid Mechanics. 699, 1-49 (2012)

23. Wu, M., Martin, M.P.: Direct Numerical Simulation of Supersonic Turbulent Boundary Layer over a Compression Ramp. AIAA Journal. 45(4), 879-889 (2007)

24. Tong, F., Li, X., Duan Y., Yu, C.: Direct numerical simulation of supersonic turbulent boundary layer subjected to a curved compression ramp. Physics of Fluids. 29(12), 125101 (2017)

25. Soldati, G., Ceci, A., Pirozzoli, S.: FLEW: A DNS Solver for Compressible Flows in Generalized Curvilinear Coordinates. Aerotecnica Missili & Spazio, (2024)

26. Lee, S., Lele, S.K., Moin, P.: Eddy shocklets in decaying compressible turbulence. Physics of Fluids A: Fluid Dynamics. 3(4), 657-664 (1991)

27. Ahn, Y.-J. Eitner, M. A., Musta, M. N., Sirohi, J., Clemens, N. T., Rafati, S.: Experimental Investigation of Flow-Structure Interaction for a Compliant Panel under a Mach 2 Compression-Ramp. American Institute of Aeronautics and Astronautics (2021). https://doi.org/10.2514/6.2022-0293

28. Fan, J., Uy, K.C.K., Hao, J. When, C.-Y.: Coexistence of different mechanisms underlying the dynamics of supersonic turbulent flow over a compression ramp. Physics of Fluids. 36(1), 016115 (2024)

29. Lee, S., Gross, A.: Numerical investigation of wall-pressure fluctuations for Mach 2 turbulent shock-wave boundary layer interactions. Physics of Fluids. 35(11), 116113 (2023)

30. Jenquin, C., Johnson, E.C., Narayanaswamy, V.: Investigations of shock–boundary layer interaction dynamics using high-bandwidth pressure field imaging. Journal of Fluid Mechanics. 961, A5 (2023)

31. Dolling, D.S.: Fluctuating Loads in Shock Wave/Turbulent Boundary Layer Interaction: Tutorial and Update. American Institute of Aeronautics and Astronautics. (2013)

32. Dupont, P., Haddad, C., Ardissone, J.P., Debieve, J.F.: Space and time organisation of a shock wave/turbulent boundary layer interaction. Aerospace Science and Technology. 9(7), 561-572 (2005)

33. Bernardini, M., Della Posta, G., Salvadore, F., Martelli, E.: Unsteadiness characterisation of shock wave/turbulent boundary-layer interaction at moderate Reynolds number. Journal of Fluid Mechanics. 954, A43 (2023)